

Pressure-driven flow past spheres moving in a circular tube

G. J. SHEARD^{1,2} AND K. RYAN¹

¹Fluids Laboratory for Aeronautical and Industrial Research (FLAIR), Department of Mechanical Engineering, Monash University, Melbourne, Victoria 3800, Australia

²Monash University Biomedical Engineering Technology Alliance (MuBeta), Monash University, Melbourne, Victoria 3800, Australia

(Received 15 September 2006 and in revised form 3 August 2007)

A computational investigation, supported by a theoretical analysis, is performed to investigate a pressure-driven flow around a line of equispaced spheres moving at a prescribed velocity along the axis of a circular tube. This fundamental study underpins a range of applications including physiological circulation research. A spectral-element formulation in cylindrical coordinates is employed to solve for the incompressible fluid flow past the spheres, and the flows are computed in the reference frame of the translating spheres.

Both the volume flow rate relative to the spheres and the forces acting on each sphere are computed for specific sphere-to-tube diameter ratios and sphere spacing ratios. Conditions at which zero axial force on the spheres are identified, and a region of unsteady flow is detected at higher Reynolds numbers (based on tube diameter and sphere velocity). A regular perturbation analysis and the reciprocal theorem are employed to predict flow rate and drag coefficient trends at low Reynolds numbers. Importantly, the zero drag condition is well-described by theory, and states that at this condition, the sphere velocity is proportional to the applied pressure gradient. This result was verified for a range of spacing and diameter ratios. Theoretical approximations agree with computational results for Reynolds numbers up to $O(100)$.

The geometry dependence of the zero axial force condition is examined, and for a particular choice of the applied dimensionless pressure gradient, it is found that this condition occurs at increasing Reynolds numbers with increasing diameter ratio, and decreasing Reynolds number with increasing sphere spacing.

Three-dimensional simulations and predictions of a Floquet linear stability analysis independently elucidate the bifurcation scenario with increasing Reynolds number for a specific diameter ratio and sphere spacing. The steady axisymmetric flow first experiences a small region of time-dependent non-axisymmetric instability, before undergoing a regular bifurcation to a steady non-axisymmetric state with azimuthal symmetry $m = 1$. Landau modelling verifies that both the regular non-axisymmetric mode and the axisymmetric Hopf transition occur through a supercritical (non-hysteretic) bifurcation.

1. Introduction

There exist numerous examples in engineering and biomedical fields where bodies suspended in a fluid are transported through a tube, including flushing solid matter from a pipe or conduit, the complex flow through annular devices such as combustion chambers and turbomachinery, and the motion of red blood cells in narrow vessels.

An early theoretical model to describe the potential flow past a sphere fixed in a tube was developed by Smythe (1961). That study proposed a relationship for an effective increase in tube length as a function of the ratio of sphere to tube radii, caused by the added resistance to the flow owing to the presence of the sphere. This relationship (revised by a factor of 3 in Smythe 1964) exhibited a near-hyperbolic increase from zero length change with zero radius ratio, to an asymptotic increase as the ratio approached unity. The elegance of the analysis aside, that model did not include assumptions of compressibility or distensibility necessary to relate the problem to most biological and some engineering applications.

Lighthill (1968) derived and investigated a model for deformable axisymmetric pellets driven by a pressure gradient through an elastic tube. The model incorporated a viscous lubricating layer, and assumed small clearances with respect to the tube walls, allowing the model to be based on the Reynolds lubrication equation. Of significant interest was the conclusion that 'necking' of the tube behind the pellet could occur, especially for negative resting clearances. Despite the flow being driven by pressure, this necking appeared similar to a peristaltic driving force, suggesting that experimental observations of such a phenomenon in capillaries may have been misinterpreted.

By extending the model of Lighthill (1968), Fitz-Gerald (1969) considered the deformation of the model red blood cells in narrow vessels. Fitz-Gerald observed that viscous shear deformed the cells into a shape more amenable to fitting through the vessels. This deformation is caused by an imbalance between the pressures developed in the viscous lubricating layer, and the pressures acting on the body away from the wall. Furthermore, for vessels with diameters in the range 5–7 μm , resistances of 4.5 to 7 times higher than Poiseuille's law predictions based on whole-blood viscosity were found. A full discussion of the viscosity of whole blood, and its variation with haematocrit (volume ratio of red blood cells to whole blood) and shear rate is beyond the scope of this paper (see Charm, McComis & Kurland 1964; Charm & Kurland 1965, 1968; Rosenson, McCormick & Uretz 1996; Long *et al.* 2004). The Fitz-Gerald (1969) study also demonstrated that deviation from axisymmetry of the pellets tended to be balanced by pressures in the flow, suggesting that the results of their axisymmetric study were valid even for non-axisymmetric pellet geometries.

The previous studies all considered the flow past a single body (sphere, spheroid, or pellet) in a tube. Tözeren & Skalak (1978) modelled the motion of a series of incompressible elastic neutrally buoyant spheres in a circular cylindrical tube, again assuming the validity of lubrication theory in the gap between body and tube wall. Tözeren & Skalak (1979), extended their model to include compressibility in the treatment of the spheres, where the sphere volume (and hence radius) was permitted to vary as a function of mean pressure acting on the sphere. They found that the linear relationship between pressure and radial deflection employed by Lighthill and Fitz-Gerald was inaccurate for elastic particles.

Deviating from the preceding assumption of axisymmetry in particle position and motion, Tözeren (1983) sought to model eccentrically positioned spheres undergoing either translational or rotational motions in tubes. The Stokes boundary-value model employed in that study permitted estimates of moments and drag forces exerted on the spheres. For small transverse displacements from the axis, drag was predicted to decrease, and the predicted decrease was more pronounced at larger sphere-to-tube diameter ratios. Unsurprisingly, given the existing solutions for the flow past an eccentrically positioned cylinder in a tube applicable to the function of valves (e.g. see Piercy, Hooper & Winney 1933), the pressure drop due to the presence of the sphere was found to decrease when the sphere displacement from the tube axis increased.

The eccentric sphere position in the tube invoked a rotation which was opposite to the direction in which it would rotate if it was rolling along the nearest wall.

The work of Smythe (1961) was extended by Cai & Wallis (1992) to describe an equispaced array of spheres in a tube. Again, only potential flows were considered, but a comprehensive range of diameter and spacing ratios was studied. A key finding from their analysis was the prediction that the effective resistance of the flow decreased with an increase in axial sphere spacing. Presumably, as the sphere spacing approaches infinity, their predicted resistances would asymptote towards the effective tube length increase predicted by Smythe (1961), though this was not verified in that study.

Prediction of the drag acting on an object moving within a tube is important as it allows the zero-drag condition to be found, which equates to the terminal-velocity equilibrium condition for the body. Tözeren & Skalak (1979) describe how their model improved the prediction of this zero-drag condition over the earlier Fitz-Gerald (1969) model. A theoretical solution for bluff disks moving in a cylinder based on an Oseen approximation (Pulley, Hussey & Davis 1996) presented data showing that in such a flow the drag increased with both the diameter ratio and the Reynolds number for a range of low non-zero Reynolds numbers. Other studies to compute the trajectory of bodies in tube flow include the work by Wang & Parker (1998), who used a boundary singularity method to model a sphere which was free to rotate as it passed down the tube. Their computations agreed with Tözeren (1983), finding a rotation direction opposite to the rolling direction of the nearest wall. Furthermore, they provided evidence to show that the lubrication theory applied in aforementioned studies deviated significantly from the computed results for sphere-to-tube diameter ratios of $\lesssim 35\%$.

The present study will focus only on rigid spherical particles in a tube, but it is worth noting that a variety of motions and deformation shapes are known to occur for elastic non-spherical bodies moving through tubes. For instance, Pozirikidis (2005) investigated various elastic shapes and their deformation, and observed that spherical ‘cells’ deformed into bullet shapes, and tended to propagate towards the centreline of the flow, whereas oblate and bi-concave shapes deformed to parachute and slipper shapes.

Despite the substantial number of studies in which the motion of spheres or similar bodies in tubes has been considered, of which the previous review is by no means all-encompassing, few direct numerical simulation (DNS) studies are reported in the literature. DNS simulation of these flows are not confined in Reynolds number, such as the low-Reynolds-number limitations of Stokes or Oseen theories, or the inviscid assumption of potential flow theory, and they permit the simulation (as opposed to modelling) of physical flow features such as viscous lubrication layers. However, they are limited in their capacity to simulate complex fluid–structure physics resulting from tube wall and body material properties, and chemical or molecular effects. These aspects of the system are typically disregarded, or at best, modelled. For instance, in a finite-element computational study, Ortega, Bristol & Savas (1998) used simulation of the flow past spheres adhering to a cylindrical tube wall to describe the flow of blood past adherent leukocytes in postcapillary blood vessels. Their simulations provided useful data for the resistance to the flow as a function of the relative position of multiple spheres, without resorting to simulation of the full distensibility, elasticity and material compressibility of the ‘cells’ and the ‘vessel walls’.

In an attempt to describe accurately the deformation from the resting shape of red blood cells moving in narrow vessels, Secomb, Hsu & Pries (1998, 2001) proposed a detailed model which included the repulsive effect of the endothelial surface layer, a region of near-wall blood plasma which excludes red blood cells owing to the presence of macromolecules. The endothelial surface layer reduces the effective diameter of the

vessels, while creating and maintaining a finite-thickness lubrication layer between moving cells and the vessel walls. Their model provided good comparison between the predicted deformed cell shapes and those observed in physiological experiments (Skalak & Branemark 1969; Vink & Duling 1996).

The present study seeks to investigate the fluid dynamics of the fundamental flow system underpinning the aforementioned studies: the motion of an array of equi-spaced spheres in a circular cylindrical tube. The primary objective is to gain an understanding of the flow dynamics and stability at the equilibrium condition where the spheres experience no axial (drag) force. However, the study will also comprehensively explore the parameter space introduced by independently varying the imposed pressure gradient on the tube and the velocity of the spheres within the tube to gain insight into the possible quasi-steady dynamics in transient sphere motion. Despite the obvious extension of this investigation to applications such as red blood cell motion in capillaries, a number of the features of these flows discussed in this review are not incorporated into the present study. These include the distensibility of the tube and sphere, and the presence of the endothelial surface-layer region.

The problem definition and introduction of geometric and dynamical parameters is provided in §2, as is a description of the numerical techniques for flow simulation and boundary treatment. Validation of the numerical code and a grid-independence study comprises §3. In §4, results from axisymmetric computations are reported, with emphasis on flow rate relative to, and forces acting on, the spheres at a range of Reynolds numbers and pressure gradients. In §5, a Landau analysis is employed to describe the nonlinear evolution of an axisymmetric Hopf instability in the flow. Linear stability analysis and three-dimensional simulations reveal the existence of a non-axisymmetric mode in §6. Section 7 discusses how changes in the geometry affect the flow, and conclusions are drawn in §8.

2. Methodology

In this section, the problem under investigation and the relevant parameters are defined, the computational method is described, and treatment of boundary conditions is discussed.

2.1. Problem formulation

The model under investigation comprises a series of equi-spaced spheres located on the axis of a circular tube of constant diameter. The spheres are moving at a constant velocity along the tube axis. Both the spheres and the tube wall are considered impermeable and rigid, and the fluid is driven by a pressure gradient.

Figure 1 illustrates the system under investigation, and identifies the repeating geometric unit upon which the system is based. Notice that because of the azimuthal symmetry of the system, the flow can be efficiently computed in cylindrical coordinates (z, r) , where z and r are the axial and radial dimensions, respectively.

Two geometric parameters are defined for this system. A spacing ratio

$$\text{SR} = S/d,$$

which can vary in the range $\text{SR} = [0, \infty)$, describes the spacing between each sphere, and a diameter ratio

$$\text{DR} = d/D, \tag{2.1}$$

which can vary in the range $\text{DR} = [0, 1]$, describes the diameter of the spheres relative to the tube diameter. The majority of the computations reported in this study are

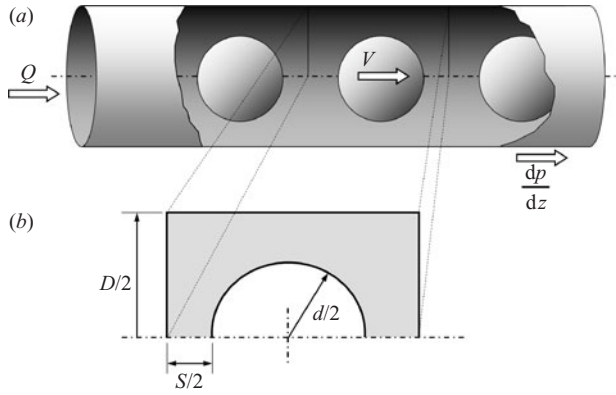


FIGURE 1. Schematic diagram of the system under investigation. (a) A series of spheres in a tube is shown, with sphere velocity (V), flow rate (Q), and pressure gradient (dP/dz) labelled. (b) The repeating axisymmetric unit is shown, with the computational domain shaded grey. The tube diameter (D), sphere diameter (d), and sphere spacing (S) are labelled.

conducted with $SR = 1.0$ and $DR = 0.6$, taken to be approximately the middle of the range of values of interest to the biological and engineering applications of the study. The length of the repeating tube unit is $L = d(SR + 1)$, or for these parameters, $1.2D$.

An expression for the volume fraction of the tube can be established by finding the volume ratios of the sphere to the tube section. The volume of the tube unit is

$$V_{tube} = \frac{1}{4}\pi D^2 d(SR + 1) = \frac{1}{4}\pi D^3(DR)(SR + 1).$$

The sphere volume is given by

$$V_{sphere} = \frac{4}{3}\pi \left(\frac{1}{2}D\right)^3 = \frac{1}{6}\pi d^3 = \frac{1}{6}\pi D^3(DR)^3,$$

and the volume fraction is then given by

$$VF = \frac{V_{sphere}}{V_{tube}} = \frac{\frac{1}{6}\pi D^3(DR)^3}{\frac{1}{4}\pi D^3(DR)(SR + 1)} = \frac{2}{3} \frac{DR^2}{SR + 1}.$$

The maximum possible volume fraction occurs when $DR = 1$ and $SR = 0$, giving $VF = 2/3$. The volume fraction is equivalent to the haematocrit in blood flow – a ratio of red blood cell volume to whole blood volume. The default parameters in this study ($SR = 1.0$ and $DR = 0.6$) provide a volume fraction $VF = 18\%$, lower than typical haematocrit values in human whole blood ($40\% - 50\%$), though capillary blood flow can be substantially lower because of streaming (plasma-rich blood being syphoned from low-haematocrit blood near the wall of larger vessels) and the presence of the endothelial surface layer.

To complete the parameterization of the system, a Reynolds number is defined as

$$Re = \frac{VD}{\nu},$$

where V is the speed of the spheres relative to the tube and ν is the kinematic viscosity of the fluid.

A restriction on the study of bodies free to move in a fluid-filled tube is that the motion is directly coupled to the tube Reynolds number and pressure gradient. In this study, the sphere velocity is held constant, allowing independent variation of the Reynolds number and imposed pressure gradient dP/dz . P is a kinematic static

pressure, defined $P = p/(\rho V^2)$, where p is static pressure, ρ is fluid density, and the quantity is non-dimensionalized by V^2 . It follows that the total volume flow rate Q is a function of both Reynolds number and pressure gradient.

2.2. Computational treatment

The fluid flows in this study are computed using a spectral-element method (Karniadakis & Sherwin 2005), with the computational domain discretized into quadrilateral elements. Following standard practice, elements are mapped onto a bi-unit square, and flow variables are computed on Gauss–Legendre–Lobatto quadrature points.

The present code was first employed in Sheard *et al.* (2007). For computations in cylindrical coordinates, the implementation follows the formulation clearly described by Blackburn & Sherwin (2004) for the incompressible Navier–Stokes equations. This investigation is interested in low-Reynolds-number flow behaviour in an axisymmetric geometry, and based on evidence from studies through similar geometries (e.g. Sherwin & Blackburn 2005), it is expected that the flows will be predominantly axisymmetric. The axisymmetric assumption greatly simplifies the numerical implementation, as only the fundamental azimuthal Fourier mode is retained, and azimuthal gradients and velocities are zero. The swirl-free axisymmetric Navier–Stokes equations in cylindrical coordinates are

$$\frac{\partial u_z}{\partial t} + \left(u_z \frac{\partial u_z}{\partial z} + u_r \frac{\partial u_z}{\partial r} \right) = -\frac{\partial P}{\partial z} + \frac{1}{Re} \left[\frac{\partial^2 u_z}{\partial z^2} + \frac{1}{r} \frac{\partial}{\partial r} \left(r \frac{\partial u_z}{\partial r} \right) \right], \quad (2.2)$$

$$\frac{\partial u_r}{\partial t} + \left(u_z \frac{\partial u_r}{\partial z} + u_r \frac{\partial u_r}{\partial r} \right) = -\frac{\partial P}{\partial r} + \frac{1}{Re} \left[\frac{\partial^2 u_r}{\partial z^2} + \frac{1}{r} \frac{\partial}{\partial r} \left(r \frac{\partial u_r}{\partial r} \right) - \frac{u_r}{r^2} \right], \quad (2.3)$$

$$\frac{\partial u_z}{\partial z} + \frac{\partial u_r}{\partial r} + \frac{u_r}{r} = 0, \quad (2.4)$$

where the advection term is shown here in convective form for simplicity (see Zang 1991, for a comparison of the possible forms the advection term can take in incompressible simulations). The axial and radial velocity components are given by u_z and u_r , respectively. For convenience, velocities have been non-dimensionalized by V , and spatial coordinates by D . This study employs a third-order backwards-multistep scheme for time integration based on a three-step operator splitting scheme (Karniadakis *et al.* 1991; Blackburn & Sherwin 2004). Following Karniadakis *et al.*, a second-order pressure boundary condition is applied on homogeneous pressure boundaries to maintain third-order accuracy of the velocity field in time. Details can be found in those papers, but briefly, the scheme is implemented through the following sub-steps:

1. First, the advection term is computed, with no boundary condition enforcement.
2. Secondly, the pressure term is computed by solution of a Poisson equation for the pressure field which projects the velocity field onto a divergence-free space. In this sub-step, high-order pressure boundary conditions (see Karniadakis, Israeli & Orszag 1991) are imposed on homogeneous boundaries, and Dirichlet pressure boundary conditions are also imposed.
3. Finally, the diffusion term is satisfied by solving a linear set of Helmholtz equations for each vector component of the velocity field. In this sub-step, Dirichlet velocity boundary conditions are imposed. The cylindrical coordinate system formulation requires that different Helmholtz equations are solved for the respective z - and r -direction velocity components.

A pleasing feature of a third-order backwards-multistep scheme was reported in Karniadakis & Sherwin (2005), where for advection–diffusion problems zero splitting

errors arise in stationary solutions. This has a significant bearing on the present work, where most of the reported solutions are time-independent.

2.3. Boundary treatment

While the problem involves spheres moving through a tube at velocity V , it is numerically convenient to compute the problem in the reference frame of one of the spheres. Therefore a zero velocity is imposed at the sphere surface, and an axial velocity component $-V$ is prescribed on the tube wall.

Along the axis, a zero radial velocity and normal gradient of pressure are both enforced. See Wu & Wu (1996) for a discussion of appropriate boundary conditions for stress-free and symmetry boundaries.

At the left and right domain boundaries, a periodic condition for velocity is imposed to satisfy the objective of simulating the flow past an infinite array of spheres. To impose the pressure gradient which drives the flow, the kinematic pressure is decomposed as

$$P = \frac{\overline{dP}}{dz}z + \tilde{P},$$

where $(\overline{dP}/dz)z$ is a contribution from a mean pressure gradient, and \tilde{P} is an axially periodic pressure field. The \overline{dP}/dz contribution is computed as a forcing term in (2.2) during the advection step, leaving the periodic component \tilde{P} to be computed in the standard fashion.

2.4. Floquet stability analysis

A linear stability analysis is used to determine the stability of steady or periodic axisymmetric flows to non-axisymmetric perturbations. Linear stability analysis proceeds on the assumption that an evolving instability in a flow \mathbf{u} can be represented by the superposition of a base flow \mathbf{U} and a small perturbation \mathbf{u}' , giving $\mathbf{u} = \mathbf{U} + \mathbf{u}'$. Equations governing the base flow and the perturbation can be generated by substituting this expression for the velocity into the Navier–Stokes equations, and omitting terms involving products of perturbation quantities as for small perturbations their contribution is negligible. This procedure produces equations which differ from the Navier–Stokes equations only in the form of the advection operator. For the base flow the standard nonlinear advection operator $-\mathbf{U}(\nabla \cdot \mathbf{U})$ is used, while for the perturbation the linear operator $-\mathbf{u}'(\nabla \cdot \mathbf{U}) - \mathbf{U}(\nabla \cdot \mathbf{u}')$ is used instead. Notice therefore that the base flow is not coupled to the perturbation field.

The evolution of the perturbation field is monitored from an initially random state over a number of base flow periods to determine the stability to perturbations of a particular azimuthal wavelength. To characterize the stability of a periodic flow the Floquet multiplier $\mu \equiv \exp(\sigma T)$ is defined, where σ is a complex growth rate, and T is the period of the base flow. Floquet multipliers describe the linear change in a perturbation over T , i.e. $F(t + T) = |\mu|F(t)$, where $F(t)$ is some quantity associated with the perturbation. In this study, this quantity was defined as the integral of azimuthal velocity magnitude throughout the computational domain,

$$F(t) = \int_{\Omega} |u'_{\theta}| d\Omega.$$

Floquet multipliers $|\mu| > 1$ describe growing (or unstable) modes. Steady flows can be considered periodic with arbitrary period T , permitting the Floquet multiplier to be used to characterize their stability. A number of methods are available to perform this analysis (e.g. see Natarajan & Acrivos 1993; Noack & Eckelmann 1994; Barkley

& Henderson 1996; Sherwin & Blackburn 2005), and in this study a one-dimensional power-type method is employed to determine the growth rate of the fastest-growing mode of a chosen azimuthal wavenumber. The power method monitors the change in magnitude of a renormalized perturbation over time T , where the perturbation is represented by a Fourier expansion of the velocity and pressure fields in the azimuth, and it is integrated in time using the linearized Navier–Stokes equations. Over a sufficient number of periods (here typically 10 to 50), all but the fastest-growing mode decay to negligible levels, and thus the change in magnitude of the perturbation relates to the magnitude of the Floquet multiplier of the instability.

This technique can distinguish real and complex-conjugate modes, and has successfully been used to identify a number of instabilities in steady and periodic axisymmetric flows (Sheard, Thompson & Hourigan 2003). Real modes are characterized by a convergence of the predicted multiplier, whereas the imaginary component of a complex-conjugate mode usually dictates that the predicted multiplier will not converge: instead it typically lies within a band of values fluctuating about some finite mean. In this study, the base flows are time-independent, allowing the period for stability analysis to be chosen as the period of the quasi-periodic instability mode. This approach achieves converged Floquet multipliers for complex modes, and provides accurate resolution of the growth rates of the instabilities.

The perturbation field is computed with zero velocity enforced on Dirichlet boundaries, and zero normal gradient of velocity enforced on homogeneous Neumann boundaries. Along the axis, a zero perturbation pressure is enforced, along with zero axial, radial and azimuthal perturbation velocity components. To allow for the possibility of flow across the axis, the mode with azimuthal wave number $m = 1$ permits non-zero radial and azimuthal velocities on the axis (for details see Blackburn & Sherwin 2004).

2.5. Three-dimensional simulations

The solver employed for the axisymmetric computations and stability analysis is also capable of performing three-dimensional simulations. Based on a Cartesian formulation of the Navier–Stokes equations, the solver performs spatial discretization using nodal hexahedral (brick) elements (for details see Karniadakis & Sherwin 2005), and a third-order backwards-multistep time-integration scheme similar to that used in the axisymmetric solver. This three-dimensional code will be employed to verify the predictions of the Floquet linear stability analysis.

3. Validation and mesh refinement

This section describes the tests used to validate the numerical algorithm, and to select appropriate meshes and element order.

3.1. Poiseuille flow

Although the numerical software package employed for this investigation was developed based on existing spectral-element algorithms and numerical integration techniques, the code itself is new. It is therefore appropriate that the code be tested against a known analytical solution to the Navier–Stokes equations appropriate to this study. On a rectangular grid representing the meridional half-plane of a circular tube, the code achieved the exact solution to the limit of numerical precision when the order of the elements was $N \geq 3$. This was expected as the analytic solution is represented by quadratic functions in the radial direction and constants in the axial direction, which can be exactly captured by the elemental Gauss–Legendre–Lobatto

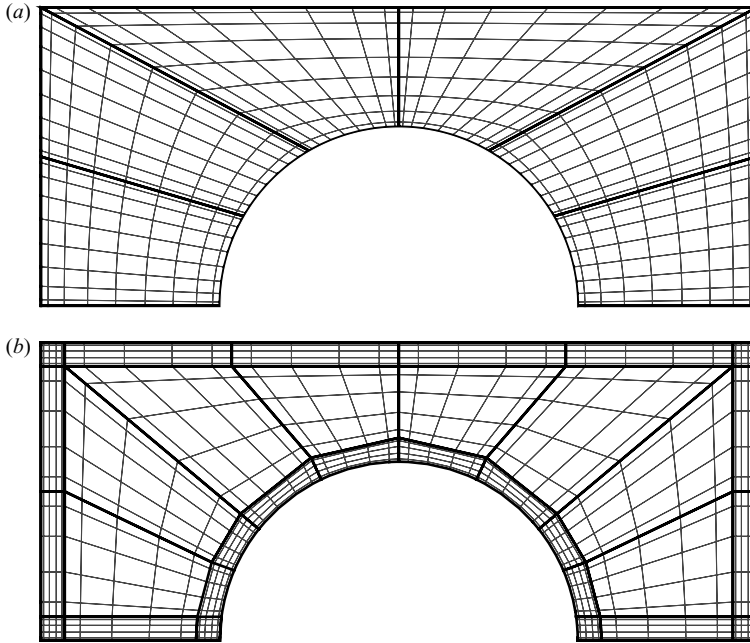


FIGURE 2. Meshes with (a) low and (b) high h -resolution. Bold lines denote macro-elements, and faint lines elucidate the spectral interpolation points within each element.

quadrature employed by the solver. This quadrature is exact for polynomials of degree $2N - 3$.

3.2. Axisymmetric and non-axisymmetric sphere flow

A more rigorous test of the code is one in which all aspects of the solver are exercised. Hence the flow past a sphere was computed to verify the capacity of the code to accurately capture complex flow phenomena such as flow separation. At Reynolds numbers $Re \approx 200$, the drag forces were compared to existing measurements (e.g. see benchmarking data in Sheard, Hourigan & Thompson 2005), and the length of the wake recirculation bubble was compared to earlier computations (Natarajan & Acrivos 1993). In each instance the code reproduced the expected results to within the accuracy of the previous studies. Computations of the flow past a sphere also provided a test case for the stability analysis code, with the estimations of the critical Reynolds number for the onset of non-axisymmetric flow from Tomboulides, Orszag & Karniadakis (1993); Johnson & Patel (1999); Ghidersa & Dušek (2000); Thompson, Leweke & Provansal (2001) being reproduced to better than 0.5 %.

3.3. Mesh selection for present study

Two mesh designs were tested for this study, and examples of these are presented in figure 2. Both the spectral elements and internal quadrature points are shown, elucidating the order of the elements. The pair of meshes were designed to test the influence of h -refinement, or the inclusion of more elements in a mesh, on the resulting solutions.

A test case was developed to examine a number of performance characteristics of the meshes and boundary treatments. This case had $SR = 1.0$ and $DR = 0.6$, mid-range values of diameter ratio and spacing to be considered in this study. Flow parameters being monitored included the flow rate relative to the sphere (Q_{rel}) and the axial drag force acting on each sphere (F_D). Q_{rel} is non-dimensionalized by $D^2 V$, and forces by $\rho V^2 D^2$.

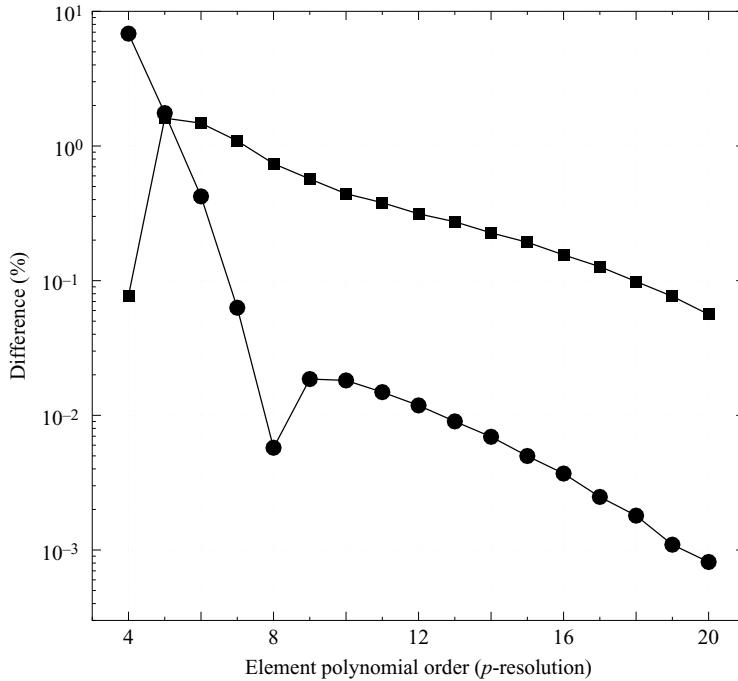


FIGURE 3. Convergence of flow rate (circles) and drag force (squares) with increasing element order (p -resolution) for the low h -resolution mesh computed with $Re = 1$, and driven by a pressure drop $\Delta P = 1$. The increasing negative slope of the data with increasing p -resolution demonstrates exponential convergence.

Figure 3 plots the results of a p -refinement (element polynomial order) study on the low h -refinement mesh; exponential convergence was obtained. The mesh with higher h -resolution was designed to resolve detailed features such as boundary layers near the tube and sphere walls. Despite the low-Reynolds-number range of applications motivating this study, a sizeable range of Reynolds numbers are to be investigated to develop fully a description of any primary axisymmetric flow transitions. The graph in figure 4 shows the p -convergence of solutions computed using the high h -resolution mesh at Reynolds numbers $Re = 1$ and 100. The plot shows that convergence rates and error magnitudes are similar for Reynolds numbers $Re = 1$ and 100, and also that superior accuracy is obtained when compared with simulations using the low h -resolution mesh with a comparable element polynomial order. Overall, the high h -resolution mesh proved more reliable, and was hereinafter used exclusively for axisymmetric computations.

A three-dimensional mesh was constructed with a similar macro-element distribution to the high- h axisymmetric mesh. A cutaway view of the mesh generated for three-dimensional computations is shown in figure 5.

4. Flow dynamics and forces on each sphere

Following a detailed grid refinement study, computations proceeded employing the high h -resolution mesh with elements of a polynomial degree sufficient to preserve a spatial error of better than 0.1% in flow rate and sphere drag measurements. The

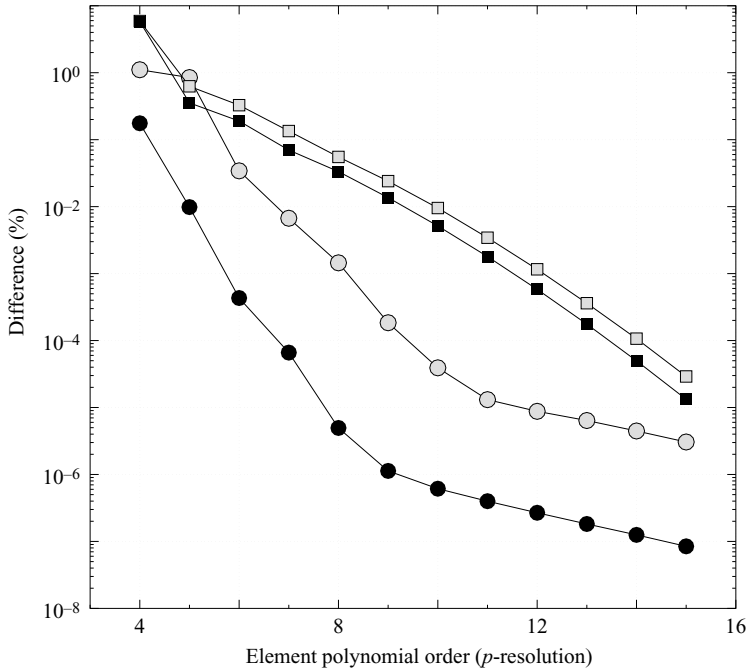


FIGURE 4. Convergence of flow rate and drag force with increasing element order (p -resolution) for the high h -resolution mesh at Reynolds numbers $Re = 1$ (solid symbols) and $Re = 100$ (open symbols). Symbols are as for figure 3.

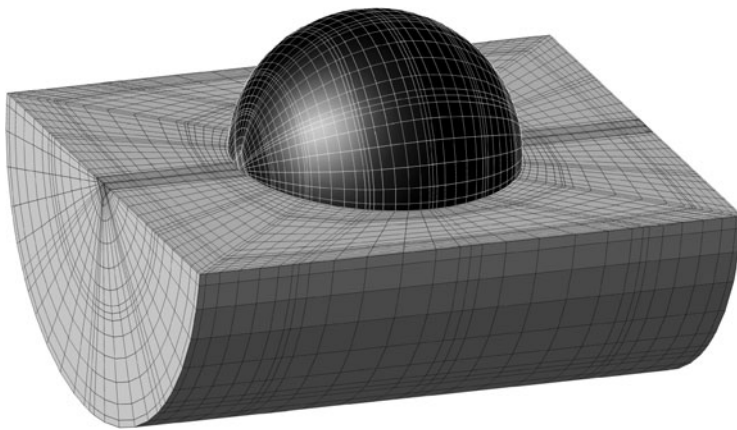


FIGURE 5. A cutaway view showing the mesh constructed for three-dimensional simulation of the flow past a sphere in a tube with a geometric configuration $DR = 0.6$ and $SR = 1$. For clarity, only the lower half of the tube is shown, revealing the mesh on the surface of the sphere.

computations reported in this section were performed exclusively for the system with a $SR = 1.0$ and $DR = 0.6$ configuration with $dP/dz = -0.8333$.

The following subsections first present computed results establishing relative flow rate and sphere drag coefficient trends for a wide range of Reynolds numbers, and then proceed to present an analysis of the low-Reynolds-number flow dynamics. The theoretical predictions are compared with the computed results.

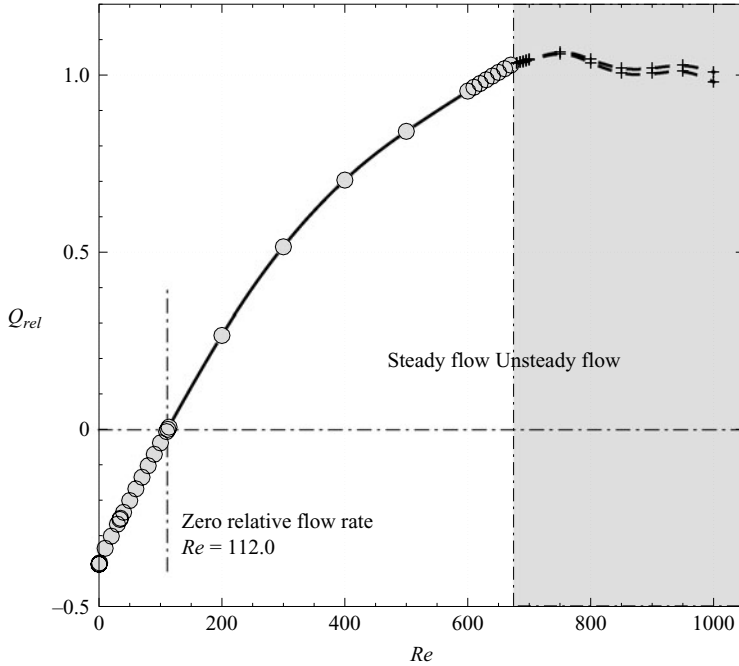


FIGURE 6. A plot of flow rate relative to spheres (Q_{rel}) against Re for a geometric configuration with $SR = 1.0$, $DR = 0.6$ and $dP/dz = -0.833\bar{3}$. The shaded region denoted the unsteady flow regime, and in this region lines through minimum and maximum values of Q_{rel} are plotted. The Reynolds number $Re = 112.0$, at which the flow relative to the sphere is zero, is highlighted.

4.1. Computed relative flow rates

The flow rate relative to the spheres is considered because it relates the pressure gradient driving the flow around the spheres to the velocity of the spheres relative to the tube, quantified by the Reynolds number. Consideration of tube flow rate also permits Reynolds numbers based on mean tube flow and sphere velocity to be related. Again for $\Delta P = 1.0$, the flow rates relative to the spheres are plotted over a wide range of Reynolds numbers in figure 6. The non-dimensional relative volume flow rate Q_{rel} is obtained by integrating the dot product of the velocity field along a boundary with the unit normal vector to that boundary. As Q_{rel} is measured relative to the translating spheres, a negative value indicates that the sphere velocity exceeds the mean fluid velocity, and vice versa for a positive value. As the pressure gradient acts in the direction of sphere motion, and only positive velocities were considered in this study, the overall flow in the tube was always positive.

The plot reveals that for Reynolds numbers $Re < 112.0$, negative relative flow rates are computed, reducing to a minimum at the limit $Re \rightarrow 0$. Below $Re \approx 250$, diffusion dominates, and the trend is approximately linear. This regime is discussed further in §4.3. Beyond $Re \approx 250$, the gradient reduces with further increases in Reynolds number until the transition to unsteady flow.

Beyond the unsteady flow transition, the envelope of the flow rate is elucidated by lines through the maximum and minimum relative flow rate values. Observe that with the onset of unsteady flow, a decrease in mean flow occurs, reflecting the transfer of energy from axial kinetic energy to radial kinetic energy in the flow. There is little difference between the maximum and minimum flow rate in the transient regime.

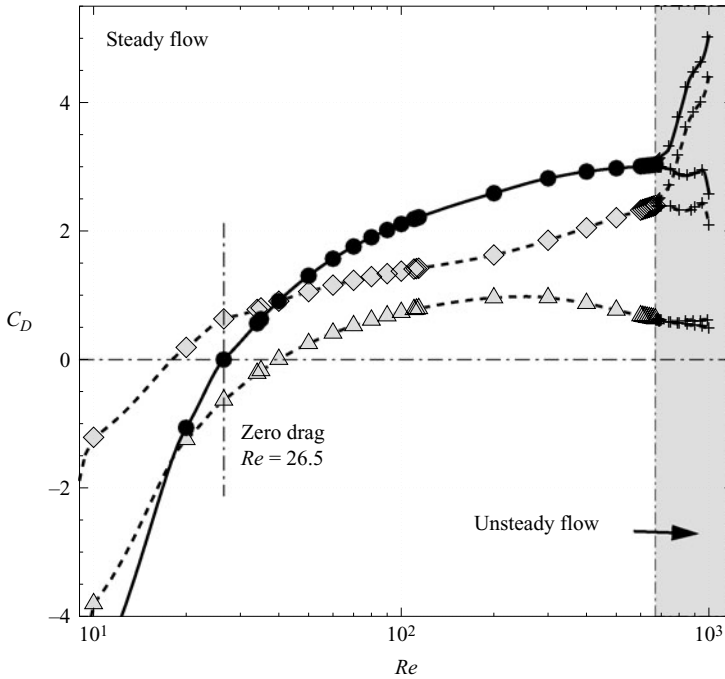


FIGURE 7. A plot of drag coefficients against Re for a geometric configuration with $SR = 1.0$, $DR = 0.6$ and $dP/dz = -0.8333$. Pressure and viscous components are shown by dotted lines and \diamond and \triangle , respectively, and the overall drag coefficient is shown by solid lines and \bullet . As for figure 6, the shading denotes the unsteady flow regime. The zero-drag condition at $Re = 26.5$ is highlighted.

Inspection of simulation results indicated that no vortex shedding was occurring in this regime; rather, a sinuous pulsing in the velocity field was detected, which did not significantly alter the general structure of the flow.

4.2. Computed sphere drag forces

The quantity of most interest in the study of spheres moving in a tube is the axial force exerted due to the sum of the pressure and viscous shear forces acting on each sphere.

It is standard practice to define a drag coefficient for a body as

$$C_D = \frac{F_D}{\frac{1}{2}\rho AU^2},$$

where F_D is the drag force, ρ is the fluid density, A is the projected frontal area of the body, and U is a reference velocity. Here the spheres have

$$A = \frac{1}{4}\pi d^2,$$

and an appropriate reference velocity is the sphere velocity V , giving

$$C_D = \frac{8F_D}{\pi\rho d^2 V^2}.$$

Plotted in figure 7 is the computed total and component drag coefficients as a function of Reynolds number. The unsteady flow regime is shaded, and the

zero-drag condition is labelled. While both the pressure and viscous drag components decrease rapidly as $Re \rightarrow 0$, interesting behaviour is observed as the Reynolds number approaches the unsteady flow transition. The viscous drag component increases up to $Re \approx 300$, before decreasing as the effect of reducing viscosity overcomes the velocity gradients at the surface of the spheres. Conversely, the pressure drag component continues to increase with Reynolds number. Beyond the onset of unsteady flow, lines through local minima and maxima of the pressure drag diverge with further increases in Reynolds number. The variation of total drag force over each oscillation cycle is almost solely due to the pressure contribution, as the viscous contribution exhibits little oscillation, suggesting that the oscillation in the flow alters the pressure field more substantially than the velocity field in the vicinity of the sphere surface.

In the steady-flow regime, a zero-drag condition is found at $Re = 26.5$. This point is of substantial physical interest as it corresponds to the equilibrium position at which a line of equispaced spheres, freely transported in a pressure-driven tube flow, would reach a uniform velocity. For this geometric configuration, the zero-drag condition occurs at a Reynolds number at which the sphere velocity exceeds the mean fluid velocity, demonstrating the role of the pressure gradient in driving this flow.

4.3. Analysis of the flow at low Reynolds number

An analysis based on a regular perturbation of the Navier–Stokes equations in powers of Reynolds number, and an application of the reciprocal theorem is now conducted to further describe the flow behaviour at low Reynolds number. It will be shown that a regular perturbation of the inertia-free creeping-flow equations truncated to $O(Re)$ provides an excellent description of the flow dynamics up to and beyond the zero-drag condition.

The creeping-flow equations for an incompressible flow can be written

$$-\nabla p + \mu \nabla^2 \mathbf{u} = 0, \quad (4.1)$$

$$\nabla \cdot \mathbf{u} = 0, \quad (4.2)$$

and a regular perturbation proceeds by taking a Taylor series expansion of the velocity and pressure fields as

$$\mathbf{u} = \mathbf{u}_0 + Re \mathbf{u}_1 + O(Re^2),$$

$$p = \frac{1}{Re} p_0 + p_1 + O(Re),$$

substituting these into (4.1)–(4.2) and boundary condition definitions for this problem, and expanding in powers of Re . Equating successive terms in the series yields a velocity field comprising a Stokes flow component (\mathbf{u}_0) satisfying

$$\nabla^2 \mathbf{u}_0 = \nabla P_0, \quad (4.3)$$

on which the Dirichlet boundary condition describing the sphere velocity is imposed, and an $O(Re)$ correction field (\mathbf{u}_1) satisfying

$$\nabla^2 \mathbf{u}_1 = \nabla P_1, \quad (4.4)$$

for which the sphere is stationary, and the applied linear pressure gradient is imposed through P_1 .

It is numerically straightforward to solve these equations subject to the divergence-free constraint (4.2). If Q_{rel0} and Q_{rel1} are the relative flow rates computed from (4.3) and (4.4), respectively, then an approximate expression for the relative flow rate takes

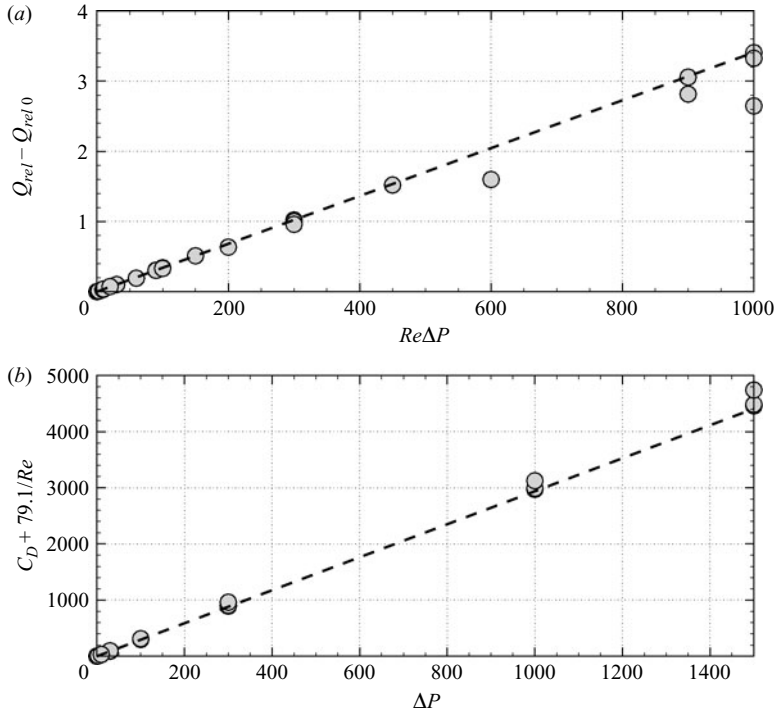


FIGURE 8. (a) $Q_{rel} - Q_{rel0}$ plotted against $Re\Delta P$. A dashed line shows the linear prediction offered by equation (4.5). (b) $C_D + 79.1/Re$ plotted against ΔP . A dashed line shows the linear prediction derived from (4.6). A total of 69 data points were computed over $0.1 \leq Re \leq 200$ and $0.1 \leq \Delta P \leq 1500$.

the form

$$Q_{rel} = Q_{rel0} + Re Q_{rel1}.$$

Numerically, the coefficients were found to be $Q_{rel0} = -0.370$ and $Q_{rel1} = 3.41 \times 10^{-3}$, when $DR=0.6$ and $SR=1$. The flow rates computed for the $O(Re)$ solution scaled linearly with ΔP , allowing the approximate expression to be written in terms of $Re\Delta P$ as

$$Q_{rel} = -0.370 + 3.41 \times 10^{-3} Re\Delta P. \tag{4.5}$$

Figure 8(a) plots data computed for a range of Re and ΔP values, and an excellent agreement between the computed flow rates and the prediction offered by (4.5) is found. The points lying below the linear trend were obtained for Reynolds numbers $Re \gtrsim O(100)$, where inertial contributions become significant.

For the drag exerted on the spheres, the Navier–Stokes equations can be used to demonstrate that the drag force will exhibit $O(Re^{-1})$ variation as $Re \rightarrow 0$: the fluctuating part of the pressure increases with Re^{-1} to balance the viscous diffusion terms, and viscous shear stresses also become proportional to Re^{-1} . Therefore, at low Reynolds numbers, a linear trend with ReC_D is expected of the form

$$ReC_D = \alpha + \Delta P Re\beta,$$

where α represents the contribution of the Stokes solution \mathbf{u}_0 , and β is a correction due to the $O(Re)$ field \mathbf{u}_1 . Again, numerical simulation was used to determine the

coefficients, yielding the approximation

$$ReC_D = -79.1 + 2.99\Delta P Re. \quad (4.6)$$

Figure 8(b) plots computed results as a rearrangement of equation (4.6) against ΔP , which is expected to yield a linear trend where the approximation is valid. The plot demonstrates that this $O(Re)$ approximation derived from the creeping-flow equations is valid for a significant range of Re and ΔP .

A useful expression for the $O(Re)$ correction coefficient in (4.6) can be determined analytically by means of the reciprocal theorem, which relates hydrodynamic forces on bodies to surface integrals over the body and the surrounding flow (see, for example, Lovalenti & Brady 1993; Magnaudet 2003; Leshansky & Brady 2004). Following Happell & Brenner (1965), the Cauchy stress tensor for an incompressible fluid may be written

$$\boldsymbol{\sigma} = -p\mathbf{I} + \mu(\nabla\mathbf{u} + \nabla\mathbf{u}^T),$$

where \mathbf{I} is the identity matrix. The reciprocal theorem relates two solutions satisfying different boundary conditions enclosed by the same surface S as

$$\int_S \mathbf{u}_0 \boldsymbol{\sigma}_1 \, d\mathbf{S} = \int_S \mathbf{u}_1 \boldsymbol{\sigma}_0 \, d\mathbf{S}, \quad (4.7)$$

where $d\mathbf{S}$ is a unit outward vector normal to the surface, and inertial contributions have been neglected. This analysis proceeds by defining the surface S as the perimeter of the meridional half-plane occupying the computational domain shown in figures 1 and 2, substituting the $O(1)$ and $O(Re)$ solutions from the regular perturbation expansion, and evaluating the contributions to the surface integrals from each boundary.

Surface integrals along the axis are zero, as the area of that surface is zero. At the sphere surface, \mathbf{u}_0 and \mathbf{u}_1 are both zero, rendering zero their contributions.

The periodic boundaries are imposed such that $\mathbf{u}_{left} = \mathbf{u}_{right}$ and $\boldsymbol{\sigma}_{0left} = \boldsymbol{\sigma}_{0right}$, so the contribution to the right-hand integral in (4.7) is zero. However, for the $O(Re)$ correction field, $\boldsymbol{\sigma}_{1left} \neq \boldsymbol{\sigma}_{1right}$ owing to the imposed pressure drop. Thus the periodic boundaries contribute the following to the left-hand side of (4.7):

$$\begin{aligned} \int_{S_{left}} \mathbf{u}_0 \boldsymbol{\sigma}_1 \, d\mathbf{S} + \int_{S_{right}} \mathbf{u}_0 \boldsymbol{\sigma}_1 \, d\mathbf{S} &= \int_{S_{left}} \mathbf{u}_0 (p + \Delta p) \mathbf{I} \, d\mathbf{S} + \int_{S_{right}} \mathbf{u}_0 p \mathbf{I} \, d\mathbf{S} \\ &= \int_{S_{left}} \mathbf{u}_0 \Delta p \mathbf{I} \, d\mathbf{S} \\ &= \Delta p \int_{S_{left}} \mathbf{u}_0 \, d\mathbf{S} \\ &= -\Delta p Q'_{rel0} \end{aligned}$$

in the axial direction, where Q'_{rel0} is the dimensional volume flow rate at zero Reynolds number.

Along the tube wall, the pressure makes a zero net contribution owing to the axisymmetry of the geometry and the flow. The right-hand integral contribution is zero as $\mathbf{u}_1 = 0$ along the tube wall, whereas the left-hand integral contribution is

$$\int_{S_{wall}} \mathbf{u}_0 \boldsymbol{\sigma}_1 \, d\mathbf{S} = \int_{S_{wall}} \langle -V, 0 \rangle \mu (\nabla\mathbf{u}_1 + \nabla\mathbf{u}_1^T) \, d\mathbf{S}.$$

In the stress tensor $\nabla \mathbf{u}_1 + \nabla \mathbf{u}_1^T$, the axial velocity gradients are zero along the wall. Continuity then requires that the radial derivative of the radial velocity is also zero, leaving an axial component

$$-V \underbrace{\left[\mu \int_{S_{wall}} \frac{\partial u_{z1}}{\partial r} dS \right]}_{F_{wall1}}. \tag{4.8}$$

The bracketed term in (4.8) corresponds to the shear force on the tube wall contributed by the $O(Re)$ correction to the low-Reynolds-number flow. The reciprocal theorem therefore states that for this system,

$$-\Delta p Q'_{rel0} - V F_{wall1} = 0. \tag{4.9}$$

F_{wall1} can be related to the body force acting on the sphere by conserving momentum in the \mathbf{u}_1 field in a finite control volume enclosing the flow domain. Eliminating inertial terms, this integral expression to be evaluated is

$$-\int_S p dS + \int_S \mu (\nabla \mathbf{u}_1 + \nabla \mathbf{u}_1^T) dS = 0.$$

Again, there is no contribution along the axis. At the periodic boundaries, only the pressure drop makes a contribution. At the surface of the sphere, the total contribution corresponds to the $O(Re)$ correction to the sphere drag force, and along the tube wall, the contribution comprises the $O(Re)$ tube wall shear force correction featuring in (4.8). Only the axial contributions are non-zero, leaving

$$\int_{S_{left}} \Delta p dS = F_{wall1} + F_{D1}. \tag{4.10}$$

Substituting into (4.9), the reciprocal theorem yields

$$-\Delta p Q'_{rel0} - V \underbrace{\int_{S_{left}} \Delta p dS}_{F_{wall1}} - F_{D1} = 0.$$

After substituting non-dimensional quantities and simplifying, this equation reduces to

$$C_{D O(Re)} = C_D - C_{D Re \rightarrow 0} \approx \Delta P \frac{8}{\pi DR^2} \left[\frac{1}{4} \pi + Q_{rel0} \right]. \tag{4.11}$$

Thus with $DR = 0.6$ and $SR = 1.0$, the relationship becomes

$$C_D + \frac{79.1}{Re} \approx 2.96 \Delta P. \tag{4.12}$$

Solving (4.12) for zero drag predicts $\Delta P Re \approx 26.7$, within 1% of the computed value. This demonstrates that this $O(Re)$ analysis accurately describes the flow at the zero-drag condition for this geometric configuration. Furthermore, when considered in dimensional form, this condition reveals that

$$V \propto \Delta p.$$

This infers that at equilibrium, the dimensional sphere velocity is proportional to the dimensional tube pressure gradient, and furthermore the constant of proportionality contains coefficients obtained only from the creeping-flow solution to (4.3).

In §7, (4.11) will be further developed to elucidate the geometry dependence of the zero-drag condition.

5. Nonlinear evolution of the axisymmetric Hopf transition

This section first describes the Landau modelling technique, which can be applied to obtain information about the nonlinear evolution of transition modes, and then describes the application of this technique to the axisymmetric Hopf transition identified in the system under investigation in this study.

5.1. Landau modelling technique

Landau modelling has been employed in numerous studies to characterize transition modes in fluid flows. Transitions can be supercritical, meaning that they exhibit no hysteresis at onset, or they can be subcritical, meaning that hysteresis is expected in the vicinity of transition. Provansal, Mathis & Boyer (1987) employed Landau modelling to determine that the first-occurring transition in the wake behind a straight circular cylinder occurs through a two-dimensional supercritical Hopf transition. Henderson & Barkley (1996) determined that the first-occurring three-dimensional instability in the wake behind a straight circular cylinder occurred through a subcritical bifurcation, in agreement with Strouhal–Reynolds-number data from experiments (Williamson 1988), which showed the existence of hysteresis at the onset of the transition.

For free-sphere wakes, Landau modelling was used by Thompson *et al.* (2001) to reveal that the first transition occurs through a regular (steady-to-steady) supercritical non-axisymmetric transition, and the subsequent transition to unsteady flow is also supercritical. Sheard, Thompson & Hourigan (2004) employed Landau modelling to characterize a range of three-dimensional and Hopf transitions behind toroidal axisymmetric bodies, identifying numerous supercritical and subcritical bifurcations.

Landau modelling assumes that the transition mode evolves nonlinearly according to the relationship

$$\frac{dA}{dt} = \sigma A + l|A|^2 A + m|A|^4 A + \dots, \quad (5.1)$$

where A is a complex oscillator whose magnitude and phase correspond to the amplitude and frequency of the evolving oscillating mode. The coefficient σ is the linear growth rate of the transition, and l , m , etc. are ‘saturation coefficients’, whose sign and magnitude determine the nonlinear saturation and character of the mode.

In the simplest application of the model, A contains only real components, requiring only the amplitude of the mode to be monitored over time. Dividing (5.1) through out by A , and recognizing that $1/A = (d/dA) \log |A|$ produces the following:

$$\frac{dA}{dt} \frac{1}{A} = \frac{dA}{dt} \frac{d \log |A|}{dA} = \frac{d \log |A|}{dt} = \sigma + l|A|^2 + m|A|^4 + \dots.$$

A plot of $d \log |A|/dt$ against $|A|^2$ can then be used to ascertain transition properties. Specifically, the y -intercept corresponds to the growth rate σ , and the gradient at the y -axis corresponds to l . A linear trend with negative gradient at the y -axis is characteristic of a supercritical transition, whereas a nonlinear trend and positive gradient at the y -axis indicates a subcritical transition, as such a trend is representative of a mode which can exhibit bi-stability (hysteresis).

The mode amplitude A can relate to any quantity that reflects the evolution behaviour of the mode, such as integral norms of the velocity field, change in the velocity at a point in the flow, or evolution of the envelope of some formerly static

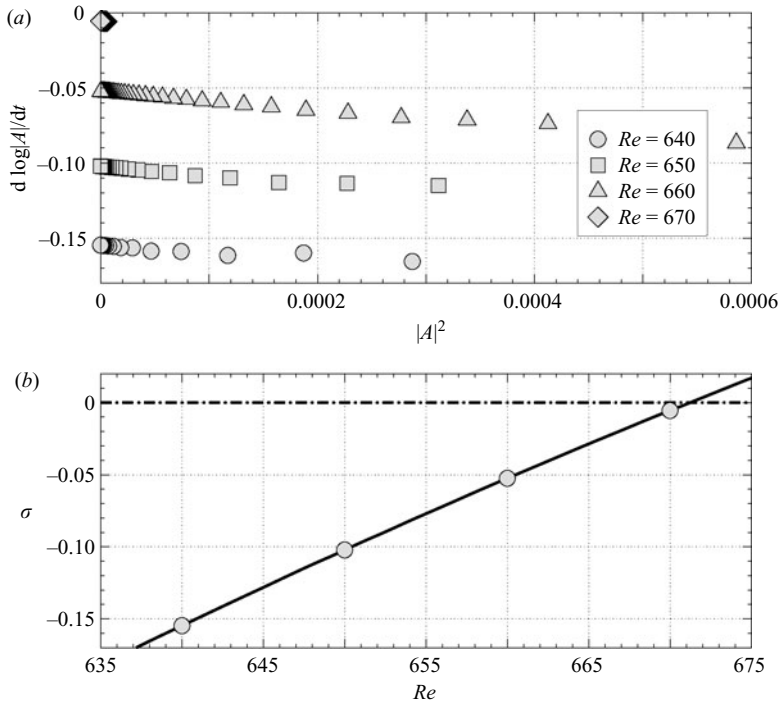


FIGURE 9. (a) Plots of $d \log |A| / dt$ against $|A|^2$ for several Reynolds numbers below the axisymmetric Hopf transition. Supercritical behaviour is demonstrated by the negative slope of the trends. (b) A plot of growth rate (σ) against Re . Extrapolation to zero growth rate yields a transition Reynolds number $Re_t = 671$.

quantity such as the drag force. Each of these is relevant providing the mode grows from a global instability (the quantities evolve in the same manner throughout the flow, Provansal *et al.* 1987). In this study, A was equated to the envelope of the oscillation of F_D acting on the sphere.

5.2. Characterizing the Hopf transition mode

A saturated unsteady solution was used as an initial field for a number of computations at Reynolds numbers in the vicinity of the transition. The amplitude time histories were obtained, and figure 9(a) shows the results of these computations.

Each data set is nearly linear, terminating at the y-axis as the modes decayed to a steady state. The negative slope and linear trends in the vicinity of the y-axis demonstrate that this Hopf transition occurs through a supercritical bifurcation: hence no hysteresis is expected to occur at onset.

Extrapolation of the trends in figure 9(a) to $|A|^2 = 0$ gives the linear growth rate σ for each Reynolds number in the vicinity of the transition. These growth rates are plotted in figure 9(b), and with extrapolation to a zero growth rate, the point of neutral stability at $Re = 671$ is obtained. This corresponds to the transition Reynolds number for the onset of unsteady flow. As described earlier, the unsteady flow emerged as a subtle pulsing of the velocity field. This critical Reynolds number was confirmed by an extrapolation to $|A|^2 = 0$ of a $|A|^2 - Re$ plot, which produced a value within 0.01 % of the value predicted from the growth rate extrapolation.

6. Non-axisymmetric flow development

The literature describes numerous studies on either the wakes behind axisymmetric bodies, or the flow through local constrictions in tubes, and in each of these flows a non-axisymmetric transition mode (azimuthal mode number $m \geq 1$) is found to emerge prior to an axisymmetric instability ($m = 0$). For example, Natarajan & Acrivos (1993) used a linear stability analysis to show that the steady axisymmetric wake behind both spheres and bluff disks in a uniform flow first become unstable to a real instability mode with azimuthal mode number $m = 1$. Likewise, Sheard *et al.* (2003) observed that the steady axisymmetric wakes behind rings with thick cross-sections first transition through a regular non-axisymmetric bifurcation. The axisymmetric wakes in that study for near-spherical rings remained steady to far higher Reynolds numbers. For confined flows in tubes, Sherwin & Blackburn (2005) found that the flow past a local stenosis contraction became unstable to a subcritical regular bifurcation also with $m = 1$. This evidence suggests overwhelmingly that the axisymmetric Hopf transition predicted in this study would be preceded by a non-axisymmetric bifurcation at a significantly lower Reynolds number, probably a regular bifurcation with azimuthal mode number $m = 1$. This section reports on linear stability analysis and three-dimensional computations which were carried out to verify the existence of such a mode.

6.1. Linear stability analysis prediction of non-axisymmetric flow transition

Linear stability analysis was performed over an extensive range of Reynolds numbers to identify instability modes associated with possible non-axisymmetric flow transitions. Several azimuthal modes were analysed, and consistently the fastest-growing azimuthal mode had a wavenumber $m = 1$, as expected. The lowest Reynolds number at which the fastest-growing non-axisymmetric mode was found to be unstable (with a Floquet multiplier exceeding the unit circle, i.e. $|\mu| > 1$) was $Re = 367$. The $m = 2$ and $m = 3$ azimuthal modes first became unstable at $Re \approx 5.2 \times 10^2$ and $Re \approx 6.1 \times 10^2$, respectively.

These predicted instabilities evolved from steady base flows, which excluded subharmonic (negative real Floquet multipliers) bifurcations. The steady base flows also permitted the magnitude of the Floquet multipliers of complex modes to be accurately computed, by using the period of the mode invoked by its imaginary component.

In figure 10, the growth rates associated with the dominant Floquet multipliers for each of the first three non-zero azimuthal modes are plotted against Reynolds number. This plot demonstrates that the first-occurring non-axisymmetric instability occurs with an azimuthal mode $m = 1$. Over a small range of Reynolds numbers $367 \lesssim Re \lesssim 384$, the flow is weakly unstable to a complex-conjugate mode, whereas for $Re \gtrsim 402$, a regular bifurcation occurs, which rapidly acquires a large growth rate.

The evolution of instability modes in a bifurcation scenario for a particular flow is known to be sensitive to geometric variation. For example, consider the different modes and the variation in onset order predicted in either square or circular cylinder wakes (Barkley & Henderson 1996; Blackburn & Lopez 2003). Likewise, the critical Reynolds numbers, and possibly the type and symmetry of the leading instabilities, may differ for pressure-driven flow past spheres in a tube with variation in either diameter ratio and sphere spacing.

Contour plots revealing the base flow vorticity field and the streamwise vorticity of the fastest-growing Floquet mode with azimuthal mode number $m = 1$ are shown in figure 11(a). The plots were obtained at $Re = 403$, just beyond the neutral stability point of the regular mode. Figure 11(b) shows the same vorticity fields plotted

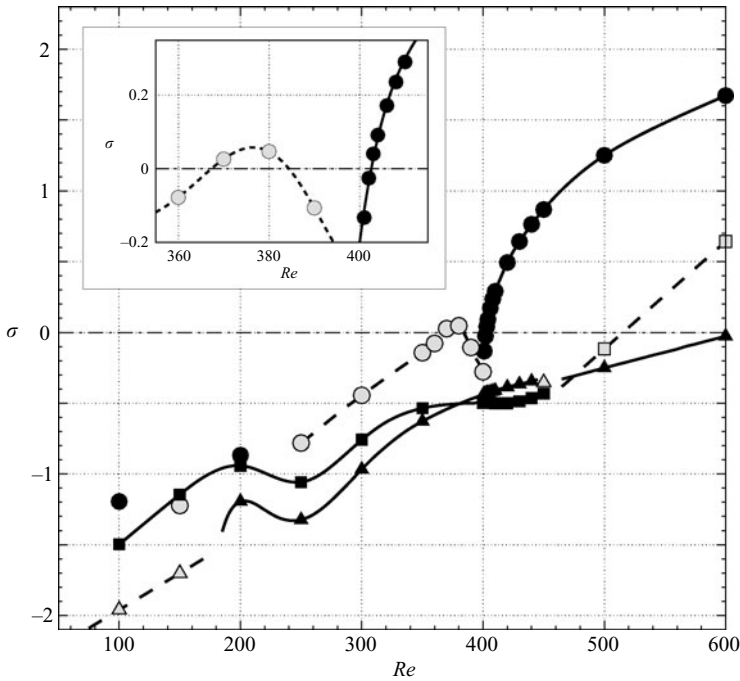


FIGURE 10. A plot of growth rate (σ) against Re for the non-axisymmetric instability modes in the flows as predicted by Floquet linear stability analysis. The growth rate was recovered from computed Floquet multipliers through $\sigma = \log(|\mu|)/T$. Azimuthal mode numbers $m = 1, 2$ and 3 are indicated by circles, squares and triangles, respectively. Dashed lines and grey symbols represent complex modes, and solid lines and symbols represent real modes. Inset: Detail of the dominant branches in the vicinity of the predicted non-axisymmetric transition.

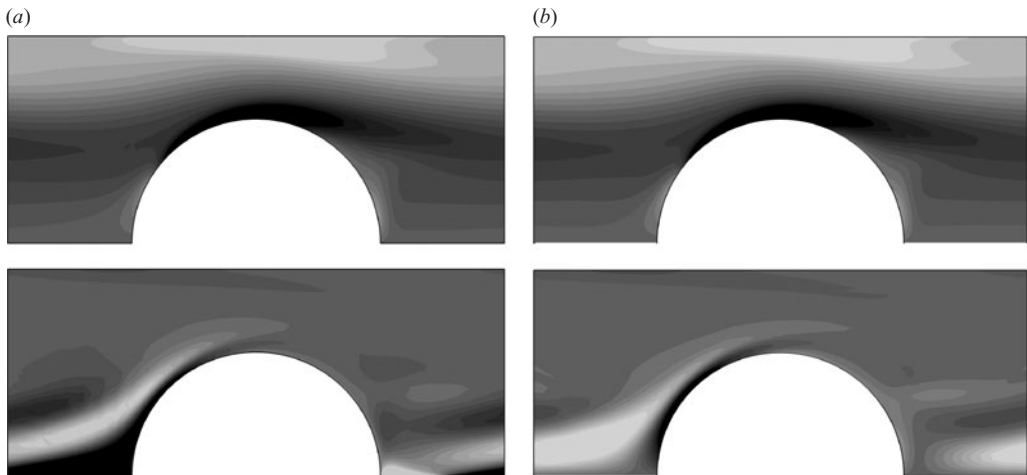


FIGURE 11. Plots of vorticity on the (z, r) -plane. (a) Azimuthal vorticity (top) of the base flow, and streamwise vorticity (bottom) of the $m = 1$ perturbation field at $Re = 403$. (b) Azimuthal (top) and streamwise (bottom) vorticity plotted on a plane extracted from the three-dimensional solution at $Re = 405$ (see figure 12). Positive and negative vorticity are shaded light and dark, respectively, and the pressure gradient is driving the flow from left to right.

Reynolds number (Re)	Symmetry	Time dependence
250, 360	Axisymmetric	Steady
380	Non-axisymmetric	Unsteady
400	Axisymmetric	Steady
405	Non-axisymmetric	Steady
≥ 410	Non-axisymmetric	Unsteady

TABLE 1. Symmetry and time-dependence of the saturated flows with $SR = 1.0$, $DR = 0.6$ and $dP/dz = -0.8333$, computed using the three-dimensional solver.

on planes extracted from a three-dimensional computation at $Re = 405$, which is reported in the section to follow. The comparison is good, and provides validation to the Floquet stability analysis solver. Only subtle differences can be detected in the out-of-plane vorticity plots, and the differences observed between the streamwise vorticity plots are due to figure 11(a) showing the form of the mode in the linear regime, whereas figure 11(b) shows a slice of the saturated non-axisymmetric mode which includes nonlinear features.

Returning to figure 11(a), the base flow vorticity field is indicative of the flow properties expected based on results reported in this paper. Local to the sphere, the base vorticity field is consistent with that of a sphere subject to a flow moving from left to right. This is in agreement with the flow-rate computations, which showed that, relative to the sphere, a net fluid flow from left to right is expected for $Re > 112.0$. Nearer to the tube wall, positive vorticity is produced owing to the motion of the sphere from left to right.

The streamwise vorticity field of the neutrally stable Floquet mode suggests that the instability develops in the flow upstream of each sphere. Near to the upstream axis, a counter-rotating vortical flow extends from just behind each sphere, gaining strength as the flow proceeds towards the next sphere, before reaching maximum strength near the forward stagnation point of each sphere, and diverting radially to follow the sphere surface. A further region of substantial perturbation field strength may be observed in the upstream region of the gap between the sphere and the tube wall.

6.2. Non-axisymmetric modes

This section reports on a validation of the Floquet stability analysis, performed using the three-dimensional solver based on hexahedral spectral elements. Computations were performed with elements of degree $N = 8$, at several Reynolds numbers in the vicinity of the predicted complex and regular bifurcations. Table 1 summarizes the results of these computations.

To verify that axisymmetry persists below $Re \lesssim 367$, simulations were performed at $Re = 250$ and 360 . Both of these simulations achieved steady-state axisymmetric solutions, with flow rates and drag forces consistent with the corresponding measurements from the axisymmetric solver.

A simulation at $Re = 380$ revealed the existence of a low-amplitude non-axisymmetric oscillation in the side forces computed on the spheres. This was consistent with the prediction that an imaginary mode was unstable for $367 \lesssim Re \lesssim 384$.

At $Re = 400$, side forces on the spheres remained negligible, suggesting that the predicted axisymmetry between the complex and regular instability regions was correct. A simulations at $Re = 405$ revealed that a steady non-axisymmetric state

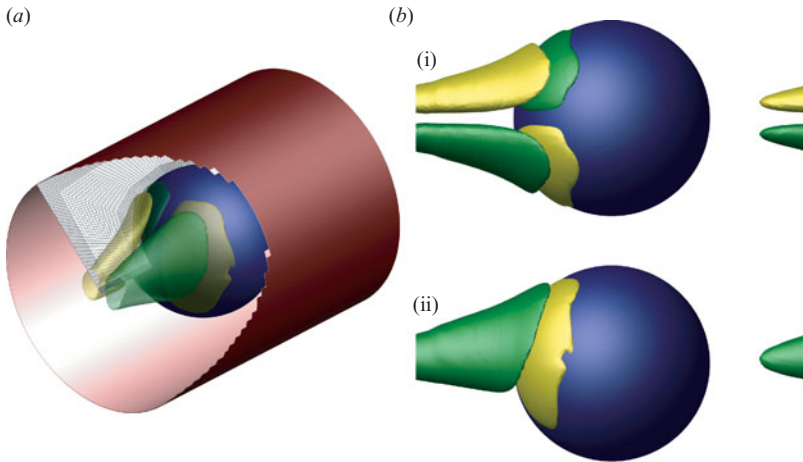


FIGURE 12. Streamwise vorticity isosurface plot for the flow around spheres in a tube at $Re = 405$ with $SR = 1.0$, $DR = 0.6$ and $dP/dz = -0.8333$. The pressure gradient is driving flow from left to right, and green and yellow isosurfaces reveal positive and negative regions of streamwise vorticity, respectively. The sphere is coloured blue, and the tube pink. (a) An isometric view, with the plane used for comparison with Floquet analysis shown in white. (b) The same structures viewed in (i) plan and (ii) elevation, with the tube removed for clarity.

emerged, consistent with the stability analysis predictions. An isosurface plot revealing the non-axisymmetric structure of the flow at $Re = 405$ is shown in figure 12. This figure also shows the orientation of the plane used to generate the plots in figure 11(b). The solution to computations at Reynolds numbers $Re \geq 410$ showed that a subsequent transition to unsteady flow developed after the initial bifurcation to non-axisymmetry. This Reynolds-number range is substantially lower than the predicted axisymmetric Hopf transition Reynolds number.

A pleasing quantitative validation between the Floquet analysis technique and the three-dimensional solver was achieved by comparing the predicted and actual growth rates of the developing regular $m = 1$ instability at $Re = 420, 440$ and 500 . The differences in growth rates were between 0.6% and 1.1% . In the three-dimensional computations, the growth rates were calculated from the growth of a transverse force component on the sphere (which must be zero in an axisymmetric flow). Application of the Landau model to this evolution revealed that the regular non-axisymmetric mode occurs through a supercritical bifurcation: that is, no hysteresis is expected in the vicinity of transition. This behaviour is consistent with that observed for the regular instability in the wake of a free sphere (Ghidera & Dušek 2000; Thompson *et al.* 2001).

The solution computed at $Re = 405$ is characterized by broad sheets of opposite-sign streamwise vorticity extending over the tube wall either side of a plane of symmetry that bisects the tube along the axis. The dominant non-axisymmetric structure within the fluid is a counter-rotating pair of opposite-sign streamwise vortices emerging at a point on each sphere near the tube wall with non-zero streamwise vorticity. These structures remain close to the reflective symmetry plane, and terminate in the vicinity of the tube axis behind each upstream sphere. Note the distinction between the counter-rotating vortex pair wake computed here, and those observed following the development of a similar regular bifurcation in the wake of a free sphere

(Johnson & Patel 1999; Thompson *et al.* 2001; Sheard *et al.* 2004). In those flows, the vortices extend far downstream of the sphere, whereas here they are obstructed by the neighbouring spheres.

7. Geometry variation

The previous sections describe in detail the flow dynamics for spheres moving in a pressure-driven fluid flow in a tube with $DR = 0.6$ and $SR = 1.0$. This section considers the cases where both of these geometric parameters are varied independently. Of particular interest is the Reynolds number at which the zero-drag condition occurs, and whether it consistently occurs in the diffusion-dominated linear regime. This information is useful in characterizing the conditions under which bodies would be carried by a pressure-driven flow in tubes where variation occurs in either the tube or particle size, or the particle concentration.

Rewriting (4.11) in terms of the total tube flow, Q , instead of the relative flow, Q_{rel} , yields

$$C_D = C_{D_{Re \rightarrow 0}} + \Delta P \frac{8}{\pi DR^2} Q_0. \quad (7.1)$$

Reynolds numbers based on sphere diameter and tube diameter are related by $Re_d = DR Re$, and therefore the $Re \rightarrow 0$ drag contribution in (7.1) can be written as

$$C_{D_{Re \rightarrow 0}} = \frac{a}{DR Re},$$

where a is a function of SR and DR .

Relationships for the zero-drag Reynolds number can be obtained by solving (7.1) equal to zero, giving

$$Re_{C_D=0} = -\frac{\pi}{8\Delta P} (DR) \left(\frac{a}{Q_0} \right), \quad (7.2)$$

or in terms of the pressure gradient,

$$Re_{C_D=0} = \frac{\pi}{8} \left(\frac{dP}{dz} \right)^{-1} \left(\frac{1}{SR + 1} \right) \left(\frac{a}{Q_0} \right). \quad (7.3)$$

The values of the coefficient a/Q_0 were computed by solving (4.3) and independently varying DR or SR . The resulting trends are plotted in figure 13. With spacing fixed at $SR = 1$, the coefficient was found to be described well by a relationship of the form

$$a/Q_0 \approx \frac{20.9}{DR - 1} - 58.2, \quad (7.4)$$

and with diameter ratio fixed at $DR = 0.6$, the coefficient obeyed the linear relationship

$$a/Q_0 = -52.5(SR + 1.14). \quad (7.5)$$

While the coefficients in these relationships were determined with $SR = 1$ (equation (7.4)) and $DR = 0.6$ (equation (7.5)), further investigation suggests that a hyperbolic relationship with DR and a linear relationship with SR are the appropriate functional forms for these relationships.

Consider for a moment the functional form of a/Q_0 with respect to SR . Combining (7.5) and (7.2)–(7.3) demonstrates that for a constant ΔP , the zero-drag Reynolds number exhibits a linear increase with SR . This occurs as a result of the linear increase

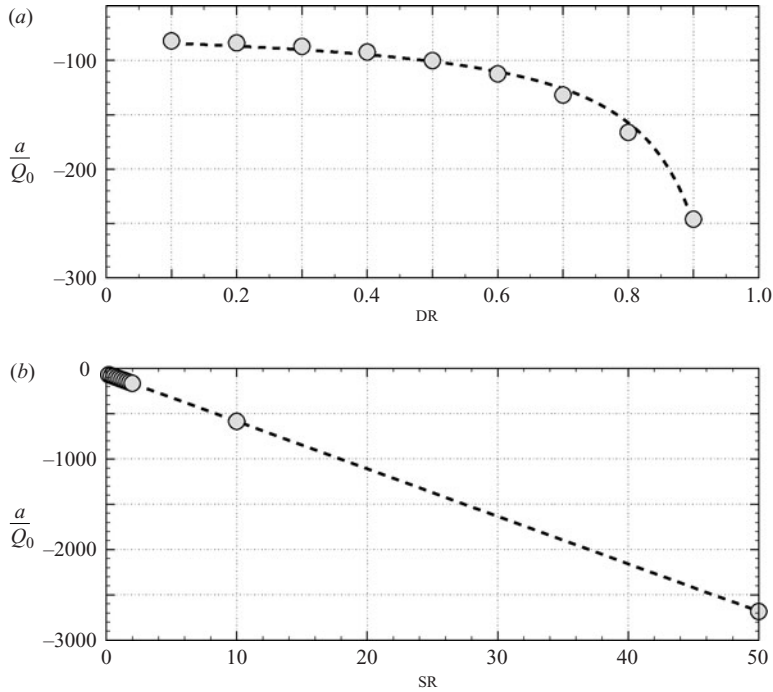


FIGURE 13. Plots of a/Q_0 against (a) DR and (b) SR. (a) $SR = 1$, (b) $DR = 0.6$. Symbols show the computed values, and dashed lines are trends according to (7.4) and (7.5) for (a) and (b), respectively.

in tube wall surface area, and therefore wall friction, that must be overcome by the pressure drop along the pipe. For large SR, it is more instructive to work in terms of the imposed pressure gradient along the pipe, and in the limit as $SR \rightarrow \infty$, a zero-drag Reynolds number $Re_{C_D=0} = 24.7$ is found for $DR = 0.6$. Note that this value depends only on the gradient of the a/Q_0 -SR relationship, as

$$\lim_{SR \rightarrow \infty} Re_{C_D=0} = \frac{8}{\pi} \left(\frac{dP}{dz} \right)^{-1} \frac{d(a/Q_0)}{d(SR)}.$$

For the case where the spheres are tightly packed, a value of $Re_{C_D=0} = 28.2$ was found as $SR \rightarrow 0$ with $DR = 0.6$.

Numerical simulations were performed to determine the zero-drag Reynolds-number behaviour with variation in either DR or SR, and the results are plotted in figure 14. The computed values are compared to predictions based on the approximate formulae proposed here, where the coefficient a/Q_0 was evaluated from the creeping-flow solution to the u_0 velocity field established in §4.3. No discernible difference between the trends was detected, verifying that for a wide range of DR and SR, the zero-drag condition is consistently dominated by viscous effects. In figure 14(b), the estimated values of the zero-drag Reynolds number at $SR = 0$ and $SR \rightarrow \infty$ are also indicated. That trend supports the analysis of Wang & Skalak (1969), who reported that the interference effects of a series of spheres in a pipe is only significant for $SR \lesssim 1$. The present study reveals that when $DR = 0.6$, a similar change in the zero-drag Reynolds number occurs over $0 \leq SR \lesssim 1$ as it does over $1 \lesssim SR < \infty$. This has

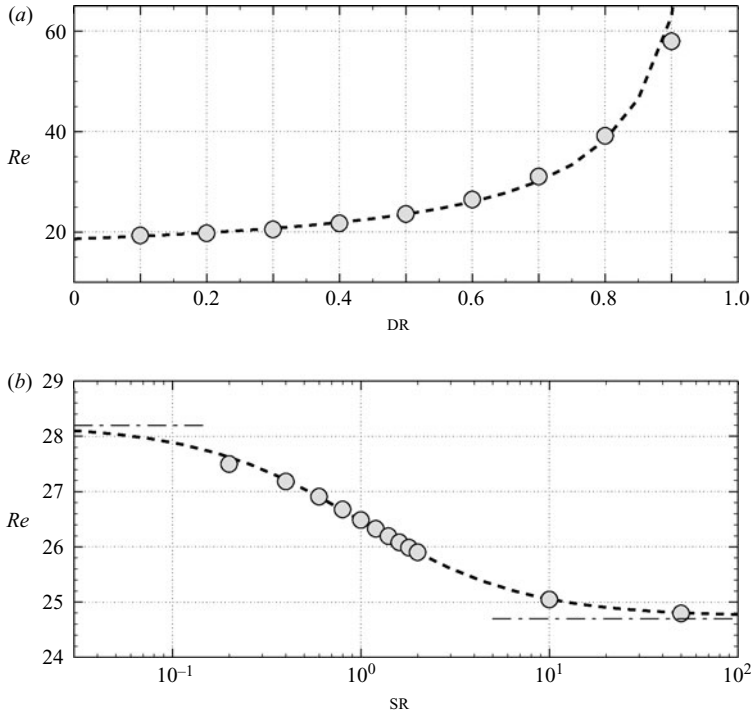


FIGURE 14. Plots of zero-drag Reynolds numbers against (a) DR and (b) SR , with the alternate parameter held constant at $SR=1$ and $DR=0.6$, respectively. A pressure gradient of $dP/dz = -0.8333$ was imposed throughout. Symbols show the computed values, and dashed lines show the trends predicted by (7.3). In (b), dash-dotted lines show the limiting values of $Re_{C_D=0}$ at $SR=0$ and $SR \rightarrow \infty$.

the implication that a line of spheres free to move in a pressure-driven tube flow will propagate at approximately the same speed in a tube of constant diameter, regardless of the sphere density over a given length.

This effect is highlighted by the vorticity contour plots provided in figure 15. Although the Reynolds number is lower than the zero-drag condition, the high region of vorticity generated by the shear flow past the sphere is consistent in shape and intensity throughout all of the SR -variation plots, and remains localized in the vicinity of the sphere. The absence of any significant impact on this high-shear region caused by the change in sphere spacing verifies the finding of spacing ratio insensitivity for the zero-drag Reynolds number.

Finally, this analysis supports a number of observations drawn from the numerical data. First, the inertial effects included in the numerical simulations appear to have a negligible influence on the flow at the zero-drag condition, for a wide range of geometric parameters and pressure gradients. Secondly, with variation in diameter ratio, a finite Reynolds number is approached as $DR \rightarrow 0$, whereas as $DR \rightarrow 1$, $Re_{C_D=0} \rightarrow \infty$, reflecting the total obstruction of the tube by the spheres. Thirdly, with variation in SR , the zero-drag Reynolds number varies from a maximum value when the spheres are touching, down to an asymptotic finite value which can be predicted based on the gradient of the a/Q_0 - SR relationship determined from a creeping-flow solution of (4.3).

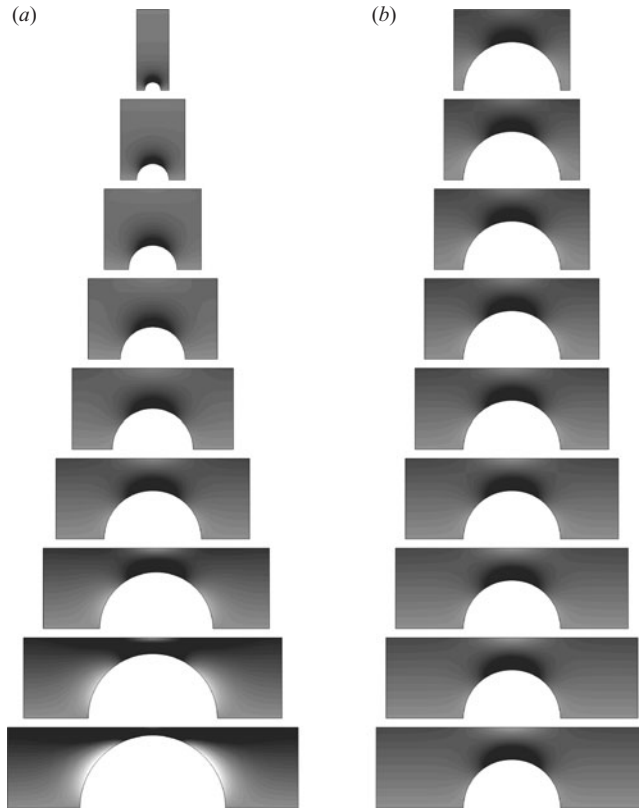


FIGURE 15. Contour plots of vorticity in the flow around spheres in tubes, with flow from left to right. (a) Diameter ratios (top to bottom) $DR = 0.1, 0.2, 0.3, 0.4, 0.5, 0.6, 0.7, 0.8$ and 0.9 for a constant spacing $SR = 1.0$. (b) Spacing ratios (top to bottom) $SR = 0.2, 0.4, 0.6, 0.8, 1.0, 1.2, 1.4, 1.6$ and 1.8 for a constant diameter ratio $DR = 0.6$. In all cases $Re = 1$ and $dP/dz = -0.8333$. Dark and light contours correspond to positive and negative vorticity, respectively.

8. Conclusions

A numerical investigation of the pressure-driven flow past a line of axially positioned equi-spaced rigid spheres moving in a tube at a fixed velocity has been presented. This study has employed a spectral-element method to compute the incompressible fluid flow. Periodic boundaries in the axial direction facilitate efficient discretization of the geometry.

With a Reynolds number based on tube diameter and sphere velocity, axial force measurements revealed that the zero-drag condition occurs at $Re = 26.5$ for a system with $SR = 1$ and $DR = 0.6$, whereas at $Re = 112$, the mean flow velocity in the tube matched the sphere velocity. These results show that for spherical bodies free to move along the axis of a pressure-driven flow, the spheres will exceed the mean fluid velocity in the tube. The numerically imposed constraint whereby the spheres are not able to rotate or translate off the axis does not invalidate the results of the study, as previous investigations tracking particles free to move within a tube flow find that spherical bodies tend to migrate towards the centreline (Pozirikidis 2005).

A regular perturbation analysis of the governing equations, combined with an application of the reciprocal theorem, provided theoretical predictions for the flow at low Reynolds number. The analysis provided an excellent prediction of the

zero-drag condition, even without the inclusion of inertial terms. It was further demonstrated that at this condition, the sphere velocity is proportional to the applied pressure gradient, where the proportionality constant contains only terms derived from creeping-flow solutions. Despite this, the theoretical trends were accurate for $Re \lesssim O(100)$.

A Landau analysis has shown that the first-occurring axisymmetric transition occurs through a supercritical Hopf bifurcation, and the onset of this transition would occur at $Re_t = 671$ for the $SR = 1$ and $DR = 0.6$ flow configuration. However, a three-dimensional linear stability analysis of this flow determines that the axisymmetric flow is weakly unstable to a complex instability mode with $m = 1$ over $367 \lesssim Re \lesssim 384$, whereas beyond $Re = 403$, a regular $m = 1$ bifurcation to non-axisymmetry occurs. This prediction was independently validated by using a three-dimensional spectral-element solver, and the emergence of a counter-rotating streamwise vortex pair in the flow was evocative of the wake behind a sphere in open flow (Natarajan & Acrivos 1993; Sheard *et al.* 2003). The regular non-axisymmetric mode was also found to occur through a supercritical bifurcation.

The zero-drag condition relating to the equilibrium condition for spheres free to travel in a pressure-driven flow in a tube is found to occur at Reynolds numbers which increase with an increase in diameter ratio DR , but are almost independent of variation in sphere spacing SR . Importantly, the sphere spacing has minimal impact on the resistance of a pressure-driven flow of spheres free to propagate in a uniform-diameter tube. The finding that the flow is highly linear at the zero-drag condition for a wide range of geometric parameters $DR = [0.1, 0.9]$ and $SR = [0.2, 50]$ could be exploited for the future development of models for the motion of bodies through tubes.

Computations were performed on the facilities of the Australian Partnership for Advanced Computing thanks to a Merit Allocation Scheme grant. The authors received salary support from the Australian Research Council through Australian Postdoctoral Fellowships (G. J. S. from ARC Discovery Project DP0555897 and K. R. from ARC Discovery Project DP0665736).

REFERENCES

- BARKLEY, D. & HENDERSON, R. D. 1996 Three-dimensional Floquet stability analysis of the wake of a circular cylinder. *J. Fluid Mech.* **322**, 215–241.
- BLACKBURN, H. M. & LOPEZ, J. M. 2003 On three-dimensional quasi-periodic Floquet instabilities of two-dimensional bluff body wakes. *Phys. Fluids* **15** (8), L57–L60.
- BLACKBURN, H. M. & SHERWIN, S. J. 2004 Formulation of a Galerkin spectral element–Fourier method for three-dimensional incompressible flow in cylindrical geometries. *J. Comput. Phys.* **197**, 759–778.
- CAI, X. & WALLIS, G. B. 1992 Potential flow around a row of spheres in a circular tube. *Phys. Fluids A* **4** (5), 904–912.
- CHARM, S. & KURLAND, G. 1965 Viscometry of human blood for shear rates of 0–100000 sec^{-1} . *Nature* **206**, 617–618.
- CHARM, S. & KURLAND, G. S. 1968 Discrepancy in measuring blood in a Couette cone and plate, and capillary tube viscometers. *J. Appl. Physiol.* **25**, 786–789.
- CHARM, S. E., MCCOMIS, W. & KURLAND, G. 1964 Rheology and structure of blood suspensions. *J. Appl. Physiol.* **19**, 127–133.
- FITZ-GERALD, J. M. 1969 Mechanics of red-cell motion through very narrow capillaries. *Proc. R. Soc. Lond. B.* **174**, 193–227.

- GHIDERSA, B. & DUŠEK, J. 2000 Breaking of axisymmetry and onset of unsteadiness in the wake of a sphere. *J. Fluid Mech.* **423**, 33–69.
- HAPPELL, J. & BRENNER, H. 1965 *Low Reynolds Number Hydrodynamics*. Prentice–Hall.
- HENDERSON, R. D. & BARKLEY, D. 1996 Secondary instability in the wake of a circular cylinder. *Phys. Fluids* **8**, 1683–1685.
- JOHNSON, T. A. & PATEL, V. C. 1999 Flow past a sphere up to a Reynolds number of 300. *J. Fluid Mech.* **378**, 19–70.
- KARNIADAKIS, G. E. & SHERWIN, S. J. 2005 *Spectral/hp Element Methods for Computational Fluid Dynamics*. Oxford University Press.
- KARNIADAKIS, G. E., ISRAELI, M. & ORSZAG, S. A. 1991 High-order splitting methods for the incompressible Navier-Stokes equations. *J. Comput. Phys.* **97**, 414–443.
- LESHANSKY, A. M. & BRADY, J. F. 2004 Force on a sphere via the generalized reciprocal theorem. *Phys. Fluids* **16** (3), 843–844.
- LIGHTHILL, M. J. 1968 Pressure-forcing of tightly fitting pellets along fluid-filled elastic tubes. *J. Fluid Mech.* **34**, 113–143.
- LONG, D. S., SMITH, M. L., PRIES, A. R., LEY, K. & DAMIANO, E. R. 2004 Microviscometry reveals reduced blood viscosity and altered shear rate and shear stress profiles in micro-vessels after hemodilution. *Proc. Natl Acad. Sci. USA* **101**, 10060–10065.
- LOVALENTI, P. M. & BRADY, J. F. 1993 The hydrodynamic force on a rigid particle undergoing arbitrary time-dependent motion at small Reynolds number. *J. Fluid Mech.* **256**, 561–605.
- MAGNAUDET, J. 2003 Small inertial effects on a spherical bubble, drop or particle moving near a wall in a time-dependent linear flow. *J. Fluid Mech.* **485**, 115–142.
- NATARAJAN, R. & ACRIVOS, A. 1993 The instability of the steady flow past spheres and disks. *J. Fluid Mech.* **254**, 323–344.
- NOACK, B. R. & ECKELMANN, H. 1994 A global stability analysis of the steady and periodic cylinder wake. *J. Fluid Mech.* **270**, 297–330.
- ORTEGA, J. M., BRISTOL, R. L. & SAVAS, O. 1998 Flow resistance and drag forces due to multiple adherent leukocytes in postcapillary vessels. *Biophys. J.* **74**, 3292–3301.
- PIERCY, N. A. V., HOOPER, M. S. & WINNEY, H. F. 1933 Viscous flow through pipes with cores. *Phil. Mag.* **15** (7), 647–676.
- POZIRIKIDIS, C. 2005 Numerical simulation of cell motion in tube flow. *Ann. Biomed. Engng* **33** (2), 165–178.
- PROVANSAL, M., MATHIS, C. & BOYER, L. 1987 Bénard–von Kármán instability: transient and forced regimes. *J. Fluid Mech.* **182**, 1–22.
- PULLEY, J. W., HUSSEY, R. G. & DAVIS, A. M. J. 1996 Low nonzero Reynolds number drag on a thin disk settling axisymmetrically within a cylindrical outer boundary. *Phys. Fluids* **8** (9), 2275–2283.
- ROSENSON, R. S., MCCORMICK, A. & URETZ, E. F. 1996 Distribution of blood viscosity values and biochemical correlates in healthy adults. *Clin. Chem.* **42**, 1189–1195.
- SECOMB, T. W., HSU, R. & PRIES, A. R. 1998 A model for red blood cell motion in glycocalyx-lined capillaries. *Am. J. Physiol. Heart Circ. Physiol.* **274**, 1016–1022.
- SECOMB, T. W., HSU, R. & PRIES, A. R. 2001 Motion of red blood cells in a capillary with an endothelial surface layer: effect of flow velocity. *Am. J. Physiol. Heart Circ. Physiol.* **281**, 629–636.
- SHEARD, G. J., THOMPSON, M. C. & HOURIGAN, K. 2003 From spheres to circular cylinders: the stability and flow structures of bluff ring wakes. *J. Fluid Mech.* **492**, 147–180.
- SHEARD, G. J., THOMPSON, M. C. & HOURIGAN, K. 2004 From spheres to circular cylinders: non-axisymmetric transitions in the flow past rings. *J. Fluid Mech.* **506**, 45–78.
- SHEARD, G. J., HOURIGAN, K. & THOMPSON, M. C. 2005 Computations of the drag coefficients for the low-Reynolds-number flow past rings. *J. Fluid Mech.* **526**, 257–275.
- SHEARD, G. J., LEWEKE, T., THOMPSON, M. C. & HOURIGAN, K. 2007 Flow around an impulsively arrested circular cylinder. *Phys. Fluids* **19** (8), 083601.
- SHERWIN, S. J. & BLACKBURN, H. M. 2005 Three-dimensional instabilities and transition of steady and pulsatile axisymmetric stenotic flows. *J. Fluid Mech.* **533**, 297–327.
- SKALAK, R. & BRANEMARK, P. I. 1969 Deformation of red blood cells in capillaries. *Science* **164**, 717–719.
- SMYTHE, W. R. 1961 Flow around a sphere in a circular tube. *Phys. Fluids* **4** (6), 756–759.

- SMYTHE, W. R. 1964 Flow around a spheroid in a circular tube. *Phys. Fluids* **7** (5), 633–638.
- THOMPSON, M. C., LEWEKE, T. & PROVANSAL, M. 2001 Kinematics and dynamics of sphere wake transition. *J. Fluids Struct.* **15**, 575–585.
- TOMBOULIDES, A. G., ORSZAG, S. A. & KARNIADAKIS, G. E. 1993 Direct and large-eddy simulation of the flow past a sphere. In *Proc. Second Intl Conf. on Turbulence Modeling and Experiments (2nd ICTME)*. Florence, Italy.
- TÖZEREN, H. 1983 Drag on eccentrically positioned spheres translating and rotating in tubes. *J. Fluid Mech.* **129**, 77–90.
- TÖZEREN, H. & SKALAK, R. 1978 The steady flow of closely fitting incompressible elastic spheres in a tube. *J. Fluid Mech.* **87**, 1–16.
- TÖZEREN, H. & SKALAK, R. 1979 Flow of elastic compressible spheres in tubes. *J. Fluid Mech.* **95**, 743–760.
- VINK, H. & DULING, B. R. 1996 Identification of distinct luminal domains for macromolecules, erythrocytes and leukocytes within mammalian capillaries. *Circ. Res.* **79** (3), 581–589.
- WANG, H. & SKALAK, R. 1969 Viscous flow in a cylindrical tube containing a line of spherical particles. *J. Fluid Mech.* **38**, 75–96.
- WANG, W. & PARKER, K. H. 1998 Movement of spherical particles in capillaries using a boundary singularity method. *J. Biomech.* **31**, 347–354.
- WILLIAMSON, C. H. K. 1988 Defining a universal and continuous Strouhal–Reynolds number relationship for the laminar vortex shedding of a circular cylinder. *Phys. Fluids* **31**, 2742–2744.
- WU, J. Z. & WU, J. M. 1996 Vorticity dynamics on boundaries. *Adv. Appl. Mech.* **32**, 119–275.
- ZANG, T. A. 1991 On the rotation and skew-symmetric forms for incompressible flow simulations. *Appl. Numer. Math.* **7**, 27–40.